

Richter, Steffen; Herrfurth, Oliver; Espinoza, Shirly; Rebarz, Mateusz; Kloz, Miroslav; Leveillee, Joshua A.; Schleife, André; Zollner, Stefan; Grundmann, Marius; Andreasson, Jakob; Schmidt-Grund, Rüdiger

Ultrafast dynamics of hot charge carriers in an oxide semiconductor probed by femtosecond spectroscopic ellipsometry

Original published in: New journal of physics / Institute of Physics. - [Bad Honnef] : Dt. Physikalische Ges.. - 22 (2020), art. 83066, 14 pp.

Original published: 2020-08-24

ISSN: 1367-2630

DOI: [10.1088/1367-2630/aba7f3](https://doi.org/10.1088/1367-2630/aba7f3)

[Visited: 2022-03-08]



This work is licensed under a [Creative Commons Attribution 4.0 International license](https://creativecommons.org/licenses/by/4.0/). To view a copy of this license, visit <https://creativecommons.org/licenses/by/4.0/>



PAPER

Ultrafast dynamics of hot charge carriers in an oxide semiconductor probed by femtosecond spectroscopic ellipsometry






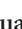





OPEN ACCESS

RECEIVED
10 March 2020REVISED
9 July 2020ACCEPTED FOR PUBLICATION
21 July 2020PUBLISHED
24 August 2020

Original content from
this work may be used
under the terms of the
[Creative Commons
Attribution 4.0 licence](#).

Any further distribution
of this work must
maintain attribution to
the author(s) and the
title of the work, journal
citation and DOI.



Steffen Richter^{1,2,7,8} , Oliver Herrfurth^{2,8} , Shirly Espinoza¹ , Mateusz Rebarz¹ ,
Miroslav Kloz¹ , Joshua A Leveillee³ , André Schleife³ , Stefan Zollner^{4,5} ,
Marius Grundmann² , Jakob Andreasson¹  and Rüdiger Schmidt-Grund^{2,6} 

¹ ELI Beamlines/Fyzikální ústav AV ČR, v.v.i., Za Radnicí 835, 25241 Dolní Břežany, Czech Republic

² Felix-Bloch-Institut für Festkörperphysik, Universität Leipzig, Linnéstr. 5, 04103 Leipzig, Germany

³ Department of Materials Science and Engineering, University of Illinois, 1304 W. Green St., Urbana, IL 61801, United States of America

⁴ Department of Physics, New Mexico State University, PO Box 30001, Las Cruces, NM, 88003-8001, United States of America

⁵ Fyzikální ústav AV ČR, v.v.i., Sekce optiky, Na Slovance 2, 18221 Praha, Czech Republic

⁶ Institut für Physik, Technische Universität Ilmenau, Weimarer Str. 32, 98693 Ilmenau, Germany

⁷ Present address: Linköpings universitet, Institutionen för fysik, kemi och biologi, 58183 Linköping, Sweden.

⁸ These authors contributed equally.

E-mail: steffen.richter@liu.se, oliver.herrfurth@physik.uni-leipzig.de and schleife@illinois.edu

Keywords: transient spectroscopy, ellipsometry, ZnO, high excitation, Mahan exciton, exciton–phonon interaction

Supplementary material for this article is available [online](#)

Abstract

Many linked processes occur concurrently in strongly excited semiconductors, such as interband and intraband absorption, scattering of electrons and holes by the heated lattice, Pauli blocking, bandgap renormalization and the formation of Mahan excitons. In this work, we disentangle their dynamics and contributions to the optical response of a ZnO thin film. Using broadband pump-probe ellipsometry, we can directly and unambiguously obtain the real and imaginary part of the transient dielectric function which we compare with first-principles simulations. We find interband and excitonic absorption partially blocked and screened by the photo-excited electron occupation of the conduction band and hole occupation of the valence band (absorption bleaching). Exciton absorption turns spectrally narrower upon pumping and sustains the Mott transition, indicating Mahan excitons. Simultaneously, intra-valence-band transitions occur at sub-picosecond time scales after holes scatter to the edge of the Brillouin zone. Our results pave new ways for the understanding of non-equilibrium charge-carrier dynamics in materials by reliably distinguishing between changes in absorption coefficient and refractive index, thereby separating competing processes. This information will help to overcome the limitations of materials for high-power optical devices that owe their properties from dynamics in the ultrafast regime.

1. Introduction

Many-body systems under non-equilibrium conditions, for instance caused by photo-excitation, still challenge the limits of our understanding at microscopic length and ultrashort time scales [1–3]. Accessing and controlling emergent states experimentally constitutes one of the most exciting, but also challenging, forefronts of contemporary materials science [4, 5]. In addition to advancing the fundamental understanding of exotic quantum states, e.g., involving large densities of free charge carriers [6, 7], understanding such many-body systems supports technological breakthroughs and the development of novel applications including high-speed optical switching [8, 9] and computing [10, 11], fast transparent electronics [12, 13], light harvesting [14, 15], or even new means of propulsion for spacecrafts [16]. The

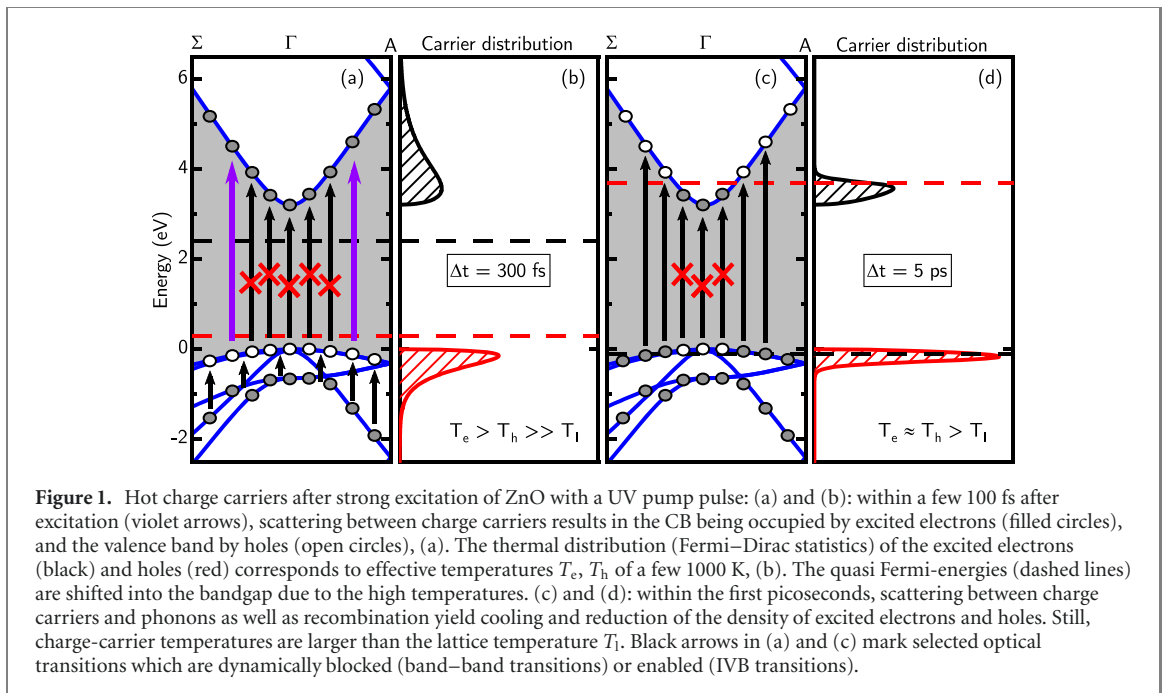


Figure 1. Hot charge carriers after strong excitation of ZnO with a UV pump pulse: (a) and (b): within a few 100 fs after excitation (violet arrows), scattering between charge carriers results in the CB being occupied by excited electrons (filled circles), and the valence band by holes (open circles), (a). The thermal distribution (Fermi–Dirac statistics) of the excited electrons (black) and holes (red) corresponds to effective temperatures T_e , T_h of a few 1000 K, (b). The quasi Fermi-energies (dashed lines) are shifted into the bandgap due to the high temperatures. (c) and (d): within the first picoseconds, scattering between charge carriers and phonons as well as recombination yield cooling and reduction of the density of excited electrons and holes. Still, charge-carrier temperatures are larger than the lattice temperature T_l . Black arrows in (a) and (c) mark selected optical transitions which are dynamically blocked (band–band transitions) or enabled (IVB transitions).

implementation of such next-generation devices requires development of techniques that probe transient states of matter and precisely control ultrafast dynamics of excited electronic systems in solids.

Many experimental and theoretical studies have aimed to separate fundamental electron–electron and electron–phonon effects, as well as the role of defect states in solids [17]. However, due to their complexity, our understanding of the coupling between fundamental electronic excitations and the lattice remains vague, especially directly after strong excitation, i.e., on short times scales after electron densities as high as 10^{20} cm^{-3} have been pumped into the CB by a fs laser pulse. As illustrated schematically in figure 1, not only the density of excited charge-carriers (as mostly probed in luminescence experiments) matters in such a highly excited regime, but also the excess energy and the distribution of charge carriers, as well as the transient electronic band structure. Therefore, the optically accessible states change rapidly, enabling or prohibiting certain absorption channels, but also changing other material properties like the index of refraction. This is especially significant for applications of transparent semiconductors like wide-gap oxides [18].

Experimentally, angular-resolved photo-electron spectroscopy is one of the most insightful probes for the dispersion of populated electronic states [19, 20]. Beyond this, optical spectroscopy accesses a convolution of joint density of states, electron and hole populations, and transition matrix elements via the complex, frequency-dependent dielectric function (DF). Conventional transient spectroscopy has been performed at different spectral ranges [21–24]. Also transient sum-frequency generation was demonstrated to probe the dynamics of electronic transitions after excitation [25]. A general challenge is to achieve not only high time-resolution but to discriminate different processes triggered by the excitation [17, 26]. In order to provide this, one must understand the entire, i.e., spectral and complex-valued, response of an excited material. This requires obtaining both, amplitude and phase information, of a sample’s DF, as encoded in its *complex* reflection coefficient \mathbf{r} .

Conventional transient spectroscopy yields only amplitudes and experimental data is often explained by changes in the extinction coefficient κ , neglecting changes of the refractive index n . This approach represents a challenge for excitation spectroscopy that has been discussed already in the 1980’s [27]. One way to compensate for the lack of phase information is to introduce restrictive model assumptions. Alternative methods are to combine measurements from different angles of incidence [28–30] or p - and s -polarization [31, 32]. However, also these methods are only work-arounds and cannot directly yield phase information. Alternative approaches to obtain the full dielectric response are heterodyne detection schemes [33] or time-domain spectroscopy. The latter, however, is only possible in the THz regime and not at optical frequencies [34].

In ellipsometry, the angles Ψ and Δ offer relative, frequency-dependent amplitude and phase information for the physical response, $\mathbf{r}_p/\mathbf{r}_s = \tan(\Psi)e^{i\Delta}$ (where indices refer to p - and s -polarizations). This provides simultaneous access to the real and imaginary part of the DF $\epsilon = \epsilon_1 + i\epsilon_2 = (n + i\kappa)^2$. In this article, we use pump-probe spectroscopic ellipsometry to obtain transient DF spectra of photo-excited ZnO

with femtosecond time-resolution. With its wide bandgap and excitons stable at room temperature [35], ZnO is an ideal testbed for this research. In particular, due to its strong polarity, the strong electron–phonon coupling also impacts exciton dynamics [36, 37].

Our ellipsometric approach based on polarization-resolved reflectance-difference measurements gives unambiguous access to the time-dependent DF of the ZnO film after excitation with about 100 fs temporal bandwidth. The experimental results yield information on the ultrafast dynamics of electron–electron and electron–phonon processes in this prototype oxide-semiconductor. They are complemented by first-principles simulations. This allows us to separate pump-induced Pauli blocking of absorption from bandgap renormalization (BGR). From our analysis we also report the direct observation of intra-valence-band (IVB) absorption. Finally, non-vanishing excitonic absorption enhancement questions the Mott transition and hints at the existence of Mahan excitons in photo-excited semiconductors.

Our experiments improve on earlier ellipsometric pump-probe studies which suffered from shortcomings such as changing positions of the probe spot on the sample or stability issues with the femtosecond lasers, or were performed only at single wavelengths (including imaging mode) [38–46].

2. Methods

We used a *c*-plane oriented ZnO thin film grown by pulsed laser deposition on a fused silica substrate. The film thickness of 30 nm is sufficient to maintain bulk properties. Only a very small excitonic enhancement due to the confinement in the thin layer is expected [47, 48]. At the same time 30 nm is thin enough to assume homogeneous excitation by a 266 nm pump pulse. We therefore do not need to consider the ambipolar diffusion of hot charge carriers. We estimate the excited electron–hole pair density to approx. $1 \times 10^{20} \text{ cm}^{-3}$. The experiment is performed at room temperature.

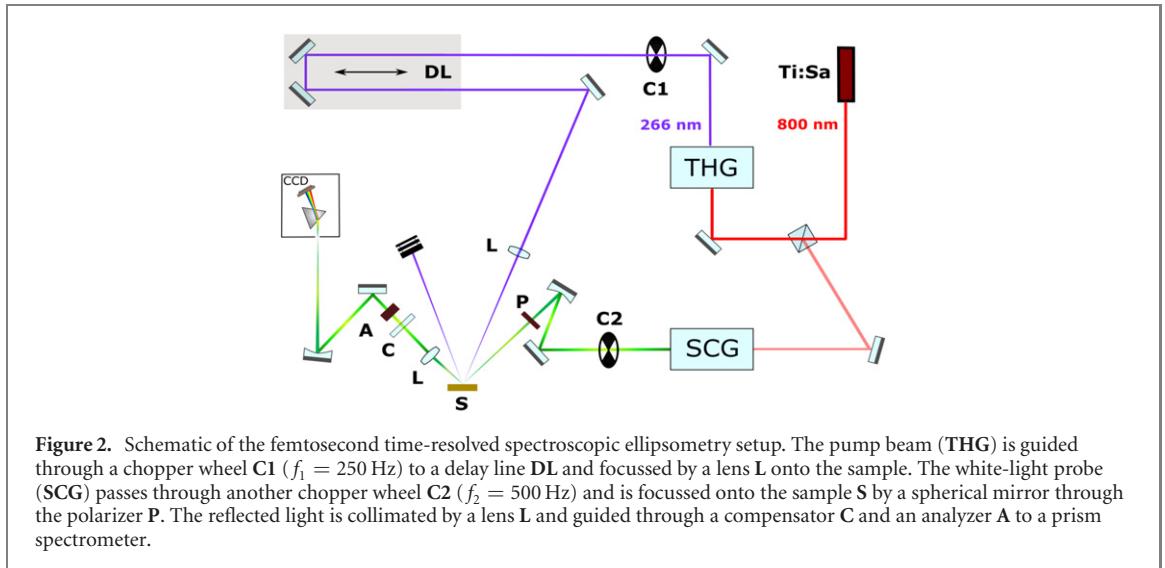
2.1. Time-resolved spectroscopic ellipsometry

We employ pump-probe spectroscopic ellipsometry, using a femtosecond pulsed laser. A schematic of the setup is shown in figure 2. Further descriptions can be found in references [49, 50]. The fundamental mode of a titanium sapphire laser (Ti:Sa) (Coherent Astrella: 35 fs, 800 nm, 1 kHz repetition rate) is used for third harmonic generation (THG, 266 nm), employed as pump beam. 1% of the laser power is used to generate supercontinuum white-light (SCG) in a CaF₂ window. In *polarizer-sample-compensator-analyzer* configuration, we measure the transient reflectance-difference signal ($\Delta R/R$)_{*j*} at 60° angle of incidence by scanning the pump-probe delay. We repeat this for ten different azimuth angles α_j of the compensator while the polarizer and analyzer are kept fixed at $\pm 45^\circ$.

Spectra were captured using a prism spectrometer and a kHz-readout CCD camera (Ing.-Büro Stresing). Most critical is the fluctuating probe spectrum and amplitude due to the CaF₂ crystal movement as well as warm-up effects at the CCD camera. Both of these problems affect the measurement mostly on time scales larger than a few milliseconds. A two-chopper scheme in the pump and probe paths is employed which allows us to obtain a wavelength-dependent live-correction for the pump-probe as well as only-probe intensity spectra, hence obtaining proper reflectance-difference spectra. In order to compute the ellipsometric parameters from the series of measurements at different compensator angles, we apply the Müller matrix formalism for each photon energy and delay time, where the obtained reflectance-difference spectra are applied to reference spectra. See supplementary information (<https://stacks.iop.org/NJP/22/083066/mmedia>) for further details⁹. The technique is comparable with a multi-channel lock-in system and enables comparison of spectra even if they have been measured long time after each other. Furthermore, it minimizes systematic errors from polarization uncertainties.

In order to minimize chirping of the probe pulse, we use a thin, broadband wire-grid-polarizer (Thorlabs) before the sample and focus the probe beam by a spherical mirror. Reflected light is analyzed by an achromatic quarter-wave plate and Glan-type prism (both Halle Nachfolger). The remaining chirp (few 100 fs difference between 2.0 eV and 3.6 eV—corresponding to roughly 3 mm dispersive material) induced by the CaF₂ as well as the support of the wire grid polarizer [31] is removed retroactively by shifting the zero-delay in the data analysis using an even polynomial for its wavelength dependence. Further details can be found in the supplementary material⁹.

⁹ Online supplementary material contains further experimental details, a Monte-Carlo-based error estimation, further characterizations of the investigated thin film sample, a group-theory discussion of dipole-allowed transitions in ZnO and further explanation about estimating the charge carrier densities, effective temperatures and plasma screening. A discussion of quasi Fermi-energies at high charge-carrier temperatures is given and the experimentally obtained DF of excited ZnO are compared to further different model-predicted ones.



The focused probe spot at the sample had a $1/e^2$ diameter of $200 \mu\text{m}$, the pump spot $400 \mu\text{m}$ (40° , s -polarized) such that lateral carrier diffusion becomes negligible [51]. The corresponding temporal and spectral bandwidths are estimated to 100 fs and 5 nm in the UV, respectively.

Modeling of the ellipsometry data to obtain the material's DF is performed using a transfer-matrix formalism [52] with the DF of ZnO parametrized by a Kramers–Kronig consistent B-spline function [53]. In the model, the film is assumed to be isotropic because the experimental configuration is mostly sensitive to the DF for ordinary polarization [54]. The model is fitted to the Mueller matrix elements N , C , S accounting also for spectral bandwidth and depolarization. The number of spline nodes was minimized in order to capture all spectral features but avoid overfitting and artificial oscillations [55]. See supplementary material for error estimation based on Monte-Carlo simulations⁹.

2.2. First-principles simulations of excited electron–hole pairs at finite temperature

We use first-principles simulations based on many-body perturbation theory to study the influence of electron–hole excitations on the optical properties of ZnO theoretically. To this end, we compute Kohn–Sham states and energies within density functional theory (DFT) [56, 57] and use these to solve the Bethe–Salpeter equation (BSE) for the optical polarization function [58]. All DFT calculations are carried out using the Vienna *ab initio* simulation package [59–61] and the computational parameters described in references [62, 63]. The influence of quasi-particle (QP) corrections on the band gap is taken into account using a scissor operator as also described in references [62, 63]. All BSE calculations are performed using the implementation described in references [64, 65].

We compute the DF as the sum of valence-conduction-band transitions $\varepsilon_{\text{DFT+QP}(N,T)}^{\text{VBCB}}$, transitions from lower valence bands into excited hole states near the valence-band maximum $\varepsilon_{\text{DFT}(N,T)}^{\text{IVB}}$, and transitions from excited electron states near the conduction-band minimum into higher CBs $\varepsilon_{\text{DFT}(N,T)}^{\text{ICB}}$, all depending on temperature T and density of excited electrons/holes N :

$$\varepsilon(N, T, E) \approx \varepsilon_{\text{DFT+QP}(N,T)}^{\text{VBCB}}(E) + \varepsilon_{\text{DFT}(N,T)}^{\text{IVB}}(E) + \varepsilon_{\text{DFT}(N,T)}^{\text{ICB}}(E) + \Delta\varepsilon_{\text{exc}}(N, E). \quad (1)$$

To compute the first three contributions, we use the independent-particle approximation, based on ground-state electronic structure and optical dipole matrix elements, and account for temperature and excitation-density dependence by means of Fermi occupation numbers of electrons and holes. Thus, Burstein–Moss shift (BMS) due to Pauli blocking is automatically included in this description. In addition, we use the model given by Berggren and Sernelius [66, 67] for doped systems at zero temperature to include the effect of BGR. BGR arises as a many-body effect due to free charge-carriers in the optically excited state and leads to a reduction of the bandgap that we include when computing $\varepsilon_{\text{DFT+QP}(N,T)}^{\text{VBCB}}(E)$. For a charge-carrier density of 10^{20} cm^{-3} by n-type doping, about 300 meV shrinkage is assumed [68]. When accounting for excitonic effects in the presence of high-temperature carriers, Fermi-distributed occupation numbers of electrons and holes need to be included also in the solution of the BSE of many-body perturbation theory. However, this turns the eigenvalue problem for the excitonic Hamiltonian into a generalized eigenvalue problem [69]. Here, we avoid this complication and increase in computational cost

and, instead, approximate excitonic effects using the zero temperature difference $\Delta\varepsilon_{\text{exc}}(N, E)$,

$$\Delta\varepsilon_{\text{exc}}(N, E) = \varepsilon_{\text{BSE+QP}(N)}(E) - \varepsilon_{\text{DFT+QP}(N)}(E). \quad (2)$$

Here, $\varepsilon_{\text{BSE+QP}(N)}(E)$ is the DF with excitonic effects and $\varepsilon_{\text{DFT+QP}(N)}(E)$ is the corresponding independent-QP DF, the band gaps for both are corrected using a scissor operator [62, 63]. While this approach neglects the influence of temperature on excitonic effects, both $\varepsilon_{\text{BSE+QP}(N)}(E)$ and $\varepsilon_{\text{DFT+QP}(N)}(E)$ include BGR and BMS.

To compute $\varepsilon_{\text{BSE+QP}(N)}(E)$, we extend the framework described in detail in references [63, 70, 71] to describe excited electrons (e) and holes (h) at a temperature of zero K. Here, the lowest CB states are occupied with free electrons of density N , and the highest valence states with holes of the same density N . Hence, transitions between these states are excluded. This is described in our framework via occupation numbers of otherwise unchanged single-particle Kohn–Sham states when computing the BSE Hamiltonian. Finally, our framework accounts for electronic interband screening of the electron–hole interaction in the BSE Hamiltonian, using the static dielectric constant obtained in independent-particle approximation, $\varepsilon_{\text{eff}} = 4.4$. In addition, as discussed earlier for doped ZnO [63], excited carriers modify the electron–hole interaction by contributing intraband screening. We approximate this contribution using the small-wave-vector limit of a static, wave-vector (q) dependent Lindhard DF, which, in the presence of free electrons and holes becomes [63, 70, 71]

$$\varepsilon_{\text{intra}}(q) \approx 1 + \frac{q_{\text{TF,e}}^2}{q^2} + \frac{q_{\text{TF,h}}^2}{q^2}, \quad (3)$$

with the Thomas–Fermi (TF) wave-vectors

$$q_{\text{TF,e/h}} = \sqrt{\frac{3Ne^2}{2\varepsilon_0\varepsilon_{\text{eff}}\tilde{E}_{\text{F}}^{\text{e/h}}}}. \quad (4)$$

The relative Fermi energies of electrons and holes at zero temperature, $\tilde{E}_{\text{F}}^{\text{e/h}}$,

$$\tilde{E}_{\text{F}}^{\text{e/h}} = \frac{\hbar^2}{2m_{\text{e/h}}} (3\pi^2 N)^{2/3}, \quad (5)$$

refer to the conduction-band minimum and valence-band maximum, $\tilde{E}_{\text{F}}^{\text{e}} = E_{\text{F}}^{\text{e}} - E_{\text{CB}}$ and $\tilde{E}_{\text{F}}^{\text{h}} = E_{\text{VB}} - E_{\text{F}}^{\text{h}}$, respectively. Equation (3) then becomes

$$\varepsilon_{\text{intra}}(q) = 1 + \frac{1}{q^2} \frac{3Ne^2}{2\varepsilon_0\varepsilon_{\text{eff}}} \left(\frac{2(m_{\text{e}} + m_{\text{h}})}{\hbar^2} \frac{1}{(3\pi^2 N)^{2/3}} \right). \quad (6)$$

$\varepsilon_{\text{intra}}$ enters the W term in the exciton Hamiltonian that is used to compute $\varepsilon_{\text{BSE+QP}(N)}$. Effective electron and hole masses are parametrized using parabolic fits to our first-principles band-structure data, leading to $m_{\text{e}} = 0.3m_0$. For the hole effective mass in equation (6) we use the geometric average of the masses of the three degenerate uppermost valence bands, i.e. $m_{\text{h}} = 0.62m_0$. This approach is valid for zero temperature of the free carriers and its implementation in our BSE code [63] allows us to compute the DF, including excitonic effects, as a function of free-charge-carrier concentration N .

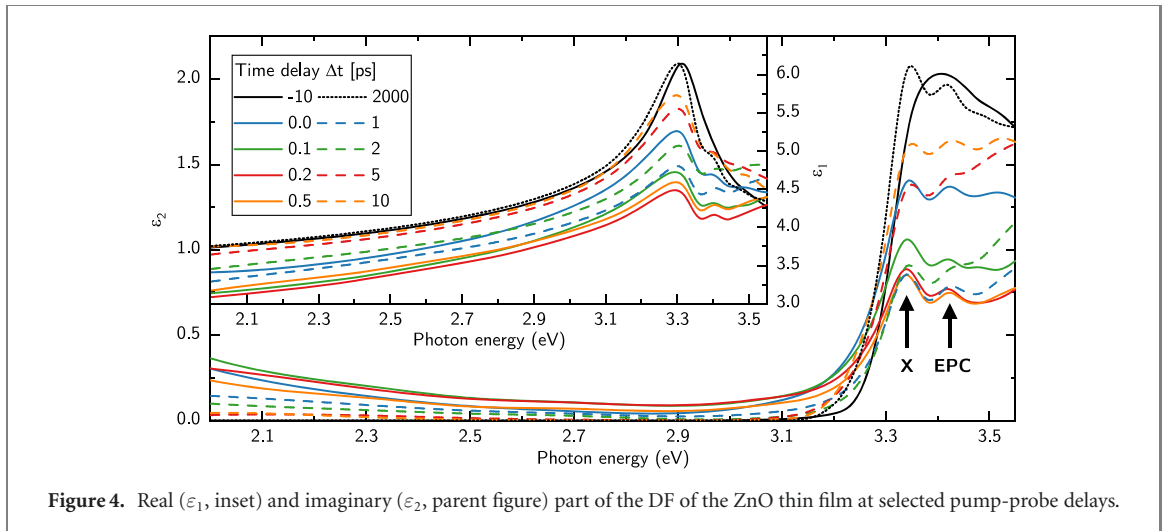
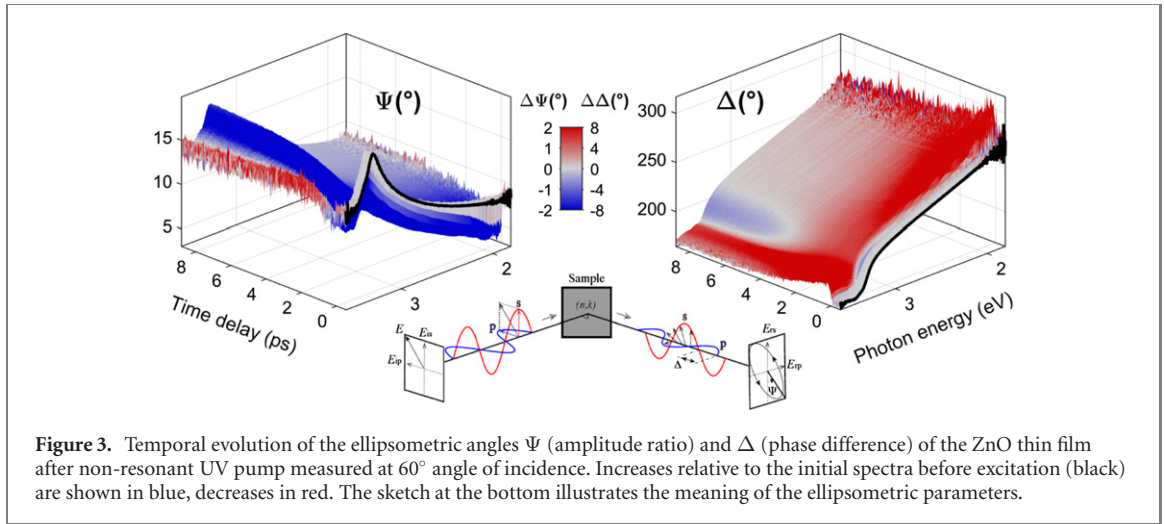
Finally, to compare with experimental pump-probe data, we compute and visualize the difference

$$\Delta\varepsilon = \varepsilon(N, T, E) - \varepsilon_{\text{BSE+QP}(N=0)}(T=0 \text{ K}, E). \quad (7)$$

3. Experimental results

The experiments were performed on a ZnO thin film, pumped by 266 nm, 35 fs laser pulses that created an electron–hole pair density of 10^{20} cm^{-3} . Supercontinuum white-light pulses were used as a probe. The transient ellipsometric angles Ψ and Δ obtained in the spectral range 1.9–3.6 eV are shown in figure 3. The uncertainty of the transient changes depends on the wavelength but is mostly on the order of 0.03° for Ψ and 0.2° for Δ . See supplementary material for comprehensive error estimation⁹. Figure 3 shows that the pump causes an immediate decrease in Ψ and an increase in Δ with spectrally and temporally varying details. Data were recorded at delays up to 2 ns with increasing delay steps.

From the ellipsometric spectra, we obtain the DF of the ZnO film for every pump-probe delay Δt . Figure 4 illustrates the resulting DF $\varepsilon = \varepsilon_1 + i\varepsilon_2$ at selected delays, and figure 5 represents transient evaluations. The uncertainty of the DF can be estimated to the order of 0.03 for ε_1 and 0.02 for ε_2 , see supplementary material⁹. At negative Δt , the obtained DF coincides with the one obtained in steady-state



ellipsometry. The peak around 3.35 eV comprises the excitonic transitions (X) and the peak around 3.42 eV is associated with exciton–phonon complexes (EPC) [36]. There exist also further complexes at slightly higher energy.

For small positive Δt , the absorption at the band edge and above is strongly damped, as indicated by the prominent decrease in ϵ_2 (figure 4). In particular, the absorption peaks of exciton and EPC are both bleached within 400 fs [red and blue symbols in figure 5(b)]. This is accompanied by a reduced refractive index below the band edge as illustrated by the concomitant drop in ϵ_1 (figure 4). Vanishing of the absorption bleaching does not start until approx. 1 ps. And we note that the excitonic enhancement does not completely vanish at any time, as indicated by the dynamics of the peak structure in ϵ_2 . Absorption recovery starts from higher energies, approaching the fundamental excitonic absorption peak only at later times. After 2 ps both the exciton and EPC absorption peaks recover with time constants of 3 ps, slowed down after 10–20 ps with a non-exponential evolution (figure 5(a)). The spectral broadening of the exciton and EPC transitions was reduced as soon as the sample has been excited (figure 4). This reduced broadening remains approximately constant for at least 2 ns.

As figure 5(c) indicates, an immediate redshift of the exciton energy by roughly 20 meV is followed by an increase with a linear rate of approx. 3 meV ps^{-1} during the subsequent 4 ps [red symbols in figure 5(c)]. The EPC follows the trend with even larger increase but without the initial redshift. Another later redshift of both yields a minimum of exciton and EPC energies at 100 ps. At 2 ns, the absorption edge remains redshifted by approx. 20 meV. It should be noted that the energetic difference between the exciton and EPC absorption peaks, which had initially increased by more than 30 meV, approaches its steady-state value (approx. 50 meV) monotonically until complete relaxation has happened after several nanoseconds [green symbols in figure 5(c)].

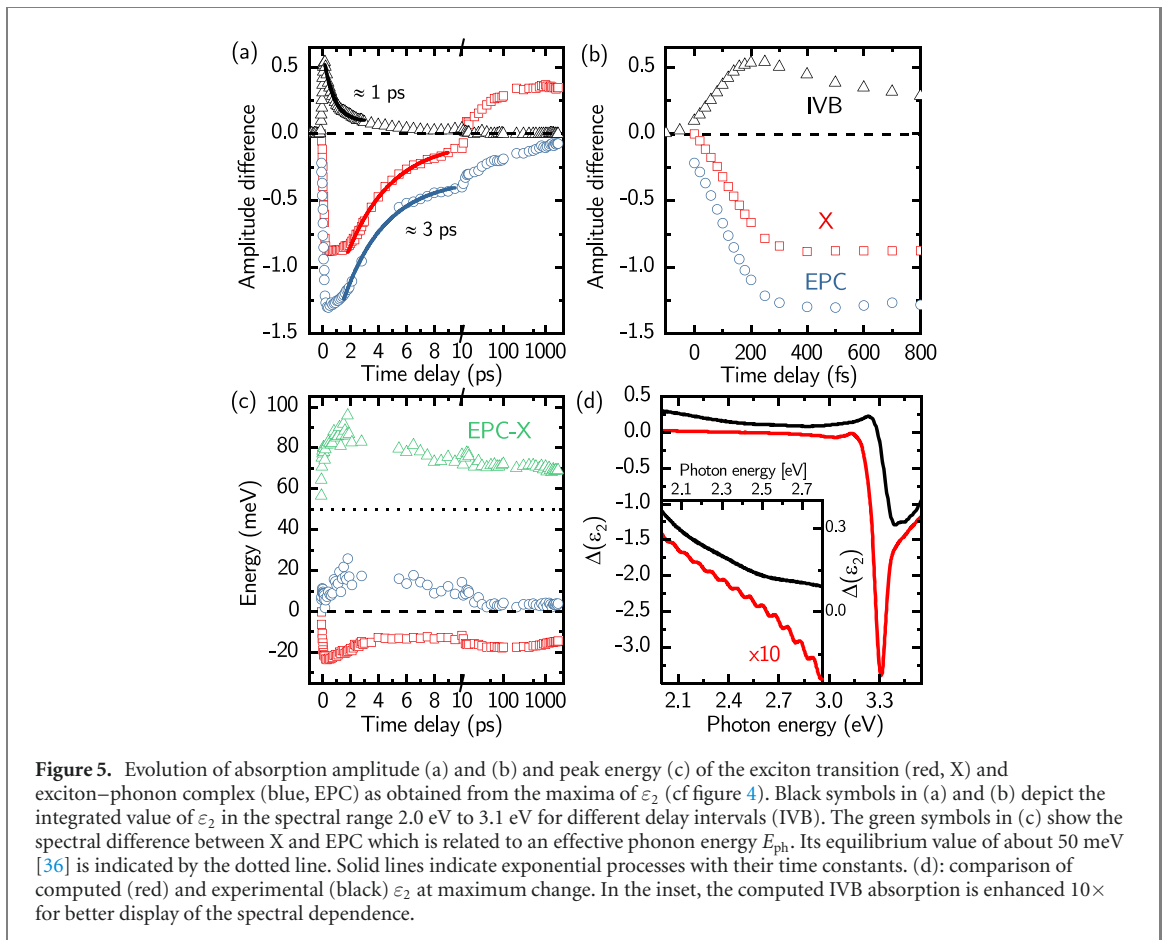


Figure 5. Evolution of absorption amplitude (a) and (b) and peak energy (c) of the exciton transition (red, X) and exciton–phonon complex (blue, EPC) as obtained from the maxima of ϵ_2 (cf figure 4). Black symbols in (a) and (b) depict the integrated value of ϵ_2 in the spectral range 2.0 eV to 3.1 eV for different delay intervals (IVB). The green symbols in (c) show the spectral difference between X and EPC which is related to an effective phonon energy E_{ph} . Its equilibrium value of about 50 meV [36] is indicated by the dotted line. Solid lines indicate exponential processes with their time constants. (d): comparison of computed (red) and experimental (black) ϵ_2 at maximum change. In the inset, the computed IVB absorption is enhanced 10× for better display of the spectral dependence.

Simultaneously with the arrival of the pump laser pulse, also a broad absorption arises at low energies in the bandgap (figure 4). This absorption reaches its maximum amplitude at $\Delta t = 0.2$ ps, and then decreases with a time constant of 1 ps. It vanishes completely after 10 ps [black symbols in figures 5(a) and (b)].

4. Discussion

4.1. Separating physical processes

Charge carrier excitation by 266 nm (4.67 eV) laser pulses in ZnO involves optical transitions from the heavy-hole, light-hole and split-off valence-bands (VB) into the conduction band (CB) in the vicinity of the Γ point, as illustrated by the violet arrows in figure 1(a). The excited electrons carry excess energies of almost 1 eV, the excited holes only about 0.4 eV because of their larger effective mass (see supplementary material⁹). Hence, while many transient spectroscopy experiments reported in the literature focus on near-resonant excitations, we induce very high excess energies to the charge carriers. The initial occupation of electron and hole states due to the pump pulse is sharply peaked and non-thermal. It takes a few hundred femtoseconds until a Fermi–Dirac distribution is established as sketched in figures 1(a) and (b). This excited state is referred to as hot charge-carriers. Estimated effective temperatures for the electrons, holes and lattice in this state are reported in table 1. Initial thermalization is provided mainly through carrier–carrier scattering and partially through carrier-phonon scattering [17, 26, 72–74]. The immediate effect of this process on the optical response spectra (figure 4) is three-fold: first, the occupation of the states leads to (partial) Pauli blocking (band filling) and hence the observed absorption bleaching of the band-to-band and excitonic transitions. This is illustrated by crossed-out black arrows in figure 1(a). An additional reduction of the excitonic absorption enhancement is expected from free-charge-carrier screening. The related reduction of the refractive index in the visible spectral range results from the Kramers–Kronig relations. Second, due to the flatness of the valence bands, excited holes have enough excess energy to scatter towards the edge of the Brillouin zone and thus promote IVB transitions [figure 1(a), short black arrows] which are observed as low-energy absorption, similar to observations for strongly doped p-type semiconductors [75, 76]. Third, the high density of photo-excited charge carriers results in BGR as seen by the redshift of the exciton energy [figure 5(c), red symbols]. Additionally, the excited carriers screen a static electric field in the film that otherwise arises from Fermi-level pinning at the

Table 1. Statistics of the electron, hole, and lattice subsystems; situation immediately after charge-carrier thermalization following a pump laser pulse with 4.67 eV that excited 10^{20} cm^{-3} electron–hole pairs in the ZnO thin film. The increase of T_1 after complete equilibration is estimated to 50 K at most. See supplementary material for details.

	Temperature (K)	Quasi Fermi-energy (meV)
Electrons	$T_e \approx 7000$	$E_F^e - E_{CB} < -660$
Holes	$T_h \approx 2800$	$E_{VB} - E_F^h < -260$
Lattice	$T_1 \approx 300$	

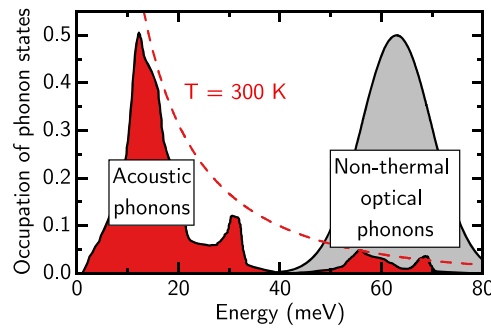


Figure 6. Simplified distribution of non-thermal (though hot) phonons after charge-carrier relaxation: the strong electron–LO–phonon interaction during cooling of the charge carriers yields a non-thermal occupation of optical phonons (gray) in contrast to the occupation of, mostly acoustic, thermal phonons (red) which follows a Bose–Einstein-distribution (red dashed line) before excitation and after lattice relaxation. The phonon density-of-states is taken from [111].

surface caused e.g. by donor-like oxygen vacancies [77]: while the observed steady-state broadening of the excitons is caused by the related band bending, pump-induced charge carriers reduce it by leveling out this band bending. At large delay times, the vacancies are still passivated by trapped electrons at the surface, thus the excitonic narrowing remains for a rather long time. Deeply trapped holes can last for microseconds [78]. We also note that the excitonic narrowing is strongly connected to the nature of the polar (*c*-plane oriented) thin film, which behaves similar to a broad quantum well with incorporated static electric field [79]. We did not observe the exciton narrowing in a non-polar *m*-plane oriented ZnO film.

Analysis of the transients yields insights into individual dynamics: charge-carrier thermalization is slightly faster for holes (200 fs) than for electrons (400 fs) because of their lower excess energy. This is observed in the experiment by a slightly shorter rise time until maximum response for the IVB absorption compared to the exciton bleaching [cf figure 5(b)]. The subsequent fast decay of the IVB absorption (figure 5(a)), is a consequence of the hole occupation far from the Γ point. Hence, its $1/e$ decay time of 1 ps reflects mainly the hole cooling by scattering with phonons. Also the transient dynamics of the absorption bleaching is governed by mainly the decrease of electron and hole temperatures: initially, electrons have much higher excess energy and hence higher effective temperature than holes (table 1). Over time, they approach each other, resulting in the situation sketched in figures 1(c) and (d). It is known that the carrier cooling occurs mainly by (polar) scattering with optical phonons [26, 37, 80, 81], and effective charge-carrier temperatures do not decrease mono-exponentially [82]. The underlying electron–LO–phonon (Fröhlich) interaction is generally very fast in polar materials, for ZnO with a Fröhlich constant α of about 1.2 [83] and $E_{LO} \approx 72$ meV, the classical scattering rate is on the order of 10^{14} Hz [84, 85]. Hence, cooling of the charge-carriers should take not longer than ≈ 0.5 ps [26]. However, here, the high excess energy of the charge carriers causes an extraordinarily large population of LO phonon states upon scattering, and thus an intermediately non-thermal phonon distribution as sketched in figure 6. A lattice temperature is not even well defined at this state. These excess phonons slow down the electron relaxation through phonon re-absorption by the charge carriers, resulting in the plateau-like transient during the first 2 ps where the relaxation is delayed [figure 5(a), blue and red symbols]. This is referred to as hot-phonon effect and was observed earlier [26, 72, 86, 87].

In general, the presence of many charge-carriers can also screen the electron–phonon interaction itself [85, 88–90]. Screening can slow down the relaxation by affecting both the Fröhlich coupling constant and the LO phonon energy [91, 92]. For 10^{20} cm^{-3} excited electron–hole pairs, we can estimate an effective plasma energy of $\hbar\omega_p \approx 0.45$ eV (parabolic approximation, see supplementary material⁹). This value exceeds the LO phonon energy by far. Hence we do not expect a dramatically altered (reduced)

electron–phonon interaction as it would occur for $\hbar\omega_p \approx E_{LO}$ [26, 91, 93]. The fact that for electrons and holes with very large excess energy, screening is not the most dominating effect in their relaxation dynamics, is also consistent with the finding that the excitonic absorption peaks do not vanish entirely (see discussion below). Finally, also the plateaus of the absorption amplitudes during the first 2 ps [figure 5(a), blue and red symbols] hint at a saturation related to hot phonons. However, the hot-phonon effect may be reduced by charge-carrier screening [26].

The non-thermal phonon distribution is also observed by the increased energetic splitting between exciton and EPC [figure 5(c), green symbols]: the effective absorption peak of the EPC at 3.42 eV is expected to involve several phonons with an effective energy E_{ph} on the order of 30 meV resulting in about 50 meV splitting [36]. The absorption and re-emission of many optical phonons by the crystal apparently increases the interaction probability of (high-energy) optical phonons with excitons while (low-energy) acoustic phonons are effectively suppressed, i.e. E_{ph} increases. After more than 2 ps the charge carriers have largely cooled down, and the number of non-thermal phonons has reached a maximum [see difference of exciton and EPC peak, figure 5(c)]. We observe that the return of the EPC absorption (vanishing Pauli blocking) has started already at times before 2 ps, i.e. slightly earlier than for the exciton absorption (figure 5(a)). This is because the occupation of energetically higher EPC states decreases faster than the occupation of states at the CB minimum and VB maximum. Lastly, we do not observe coherent phonon oscillations [94–97] because our pump energy is highly non-resonant with the band gap and well above our spectral probe window.

Effects of the high charge-carrier densities can be distinguished from the thermal excess: A reduction of the total number of excited charge carriers is observed by the vanishing BGR within the first picoseconds [cf exciton peak energy in figure 5(c)]. In the subsequent picosecond regime, we expect also the recovery of the exciton and EPC absorption to result from the reduction of the excited carrier density. This recombination is initially maintained mainly by nonradiative Auger and defect recombination [98]. We find an initial time constant of 3 ps (figure 5(a)). At later times with lower remaining carrier densities, slower radiative electron–hole recombination becomes dominant.

Thermal equilibration with the lattice can be estimated to be accomplished approx. 100 ps after the excitation when the exciton energy reaches another minimum [see figure 5(c), red symbols] that indicates the highest achieved lattice temperature and thus bandgap shrinkage [99]. Assuming a deposited energy density of 100 J cm^{-3} by the pump pulse, a maximum temperature increase of 30–50 K can be expected. If transferred entirely to the lattice, this would correspond to a bandgap decrease of approx. 25–30 meV at most. This matches the experimental observation. The following slow (approx. $2 \mu\text{eV ps}^{-1}$) heat dissipation lasts until at least 10 ns. It should be noted that the observed overshooting of the exciton amplitude at later time is related to the reduced exciton broadening as discussed above.

4.2. Interpretation

To complement our experimental results, we use first-principles electronic-structure calculations to explain the different effects near the band edge: (i) many-body perturbation theory is used to describe excitonic effects. It includes additional screening and Pauli blocking due to the high density of electrons in the conduction and holes in the valence band at 0 K temperature. (ii) The high effective temperatures of excited electrons and holes are taken into account via Fermi-distributed occupation numbers in the absorption spectrum of non-interacting electron–hole pairs.

A comparison with the experimental data in figure 5(d) shows that the observed reduction of the exciton absorption is only about half of what is expected from the calculations. An increased number of free charge carriers is known to have two opposing effects on the band-edge absorption: while the exciton is screened and should shift toward higher energies due to a reduced binding energy, the bandgap shrinks due to BGR. Both compensate each other in a good approximation, such that the absolute exciton energy remains constant [100–103]. However, when surpassing the so called Mott transition, excitons should cease to exist, and BGR should take over. That could explain the initial redshift (figure 5(c)) which has been observed earlier [30, 103, 104]. Nevertheless we find that the excitonic absorption peak does not vanish entirely at any time. That reflects the difference between an equilibrated system and hot charge carriers: in the case of doping ZnO by 10^{20} cm^{-3} excess electrons, a Burstein–Moss blueshift of the absorption edge of approximately 370 meV can be estimated from band-structures and band dispersions computed using DFT. It is clear that this does not apply to a hot electron–hole plasma where no strong blueshift is observed [27, 103, 104]. Also BGR, which should generally not depend on temperature [105], was found slightly less efficient for hot charge carriers [102]. Hence, due to the widely-distributed hot carriers, it is possible that the Mott transition does not occur despite the fact that the total density of excited charge carriers is well beyond the classical threshold [106]. According to [107], the fraction of photo-excited charge carriers bound to excitons is rather small, not exceeding 15%. In this respect, the non-vanishing exciton absorption

peaks could indicate that the occupation of the exciton ground-state would never exceed the Mott density even if 10^{20} cm^{-3} electron–hole pairs are excited. While comparisons of charge-carrier densities do not account for the effective carrier temperatures, the Mott transition can also be considered in terms of the Debye screening lengths [105]. Here, we obtain screening lengths on the order of 3 Å, which is much smaller than the exciton Bohr radius of about 2 nm in ZnO [107]. Hence, effectively uncorrelated electron and hole states should dominate (see supplementary material for details⁹). On the other hand, not only interaction lengths matter but also relevant electron (and hole) wave vectors must be similar to the TF wave-vectors for effective screening [91]. Considering the strong effect of non-parabolicity at the high excess energies of the photo-excited electrons and holes in our experiment, this can give rise to a reduced screening effect (see supplementary material for details⁹). Albeit largely screened and broadened, electron–hole coupling has indeed been observed to sustain the apparent Mott transition as so called Mahan excitons [102, 108–110], in particular also ZnO has been considered [63]. Narrow exciton-like peaks have been observed well above the Mott transition in highly-doped GaN [6], Cooper-pair signatures at the Fermi sea in highly-excited ZnO [7]. We conclude that the remaining absorption peaks that we observe in our experiment are likely to be Mahan excitons [63, 108]. While they were originally studied in degenerately doped semiconductors, our photo-excitation generates at the same time electrons in the CB and holes in the valence band.

The obvious explanation for photo-induced absorption at lower photon energies would be free carriers [112]. However, two Drude terms to describe free electrons and holes with the known densities and reasonable effective masses and mobilities cannot mimic the shape of the dispersion of the DF well. Furthermore, there are indications of a maximum of ε_2 around 1.9 eV and 2.1 eV (cf figure 4) hinting at IVB transition at the *M* point. In a recent report, similar absorption features, induced by lower pump power and at much longer time scales, were attributed to defect states [78]; however, defects can hardly explain the large absorption cross sections (ε_2) that we observe here. Effects of defects in ZnO can vary strongly between different samples [113]. To quantify absolute contributions of both effects, a detailed study of the dependence of this absorption on the photo-induced charge-carrier density would be needed but is beyond the scope of this article. However, we saw indications for lower induced absorption if a lower density of charge-carriers was created, thus absorption due to IVB should be the dominant process here. A comparison between experimental and first-principles data for $\Delta(\varepsilon_2)$ below 3 eV in figure 5(d) (inset) shows good agreement in the line shape of measured and calculated spectral features. The sub-gap energy-range between 2 and 3 eV is dominated by contributions from IVB transitions that become allowed in the presence of free holes. The computational results do not account for phonon-assisted processes, which likely explains why the computational data underestimates the experiment at these energies. Inter–CB transitions do not significantly contribute in this energy range. The appearance of the low-energy absorption indicates that the spectral weight of absorption is transferred from the fundamental absorption edge to lower energies because the total number of charge carriers remains constant, which is known as the sum rule [114].











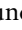
5. Conclusion

The development of fs-time-resolved spectroscopic ellipsometry allows unambiguous determination of the complex, frequency-dependent DF with sub-ps temporal resolution in a wide spectral range. It is hence a unique tool to study the dynamics of electronic systems in solids that beats conventional transient spectroscopy in several areas. Investigating a UV-pumped ZnO thin film, we were able to discriminate different processes of the non-equilibrium charge-carrier dynamics of this strongly photo-degenerate semiconductor. In contrast to previous experiments, we are able to largely minimize risks for mis-interpretations that can originate from mixing effects of changed absorption and refractive index. We observe partial blocking and screening of near-band-edge and exciton absorption due to occupation of the electronic states. A non-vanishing excitonic absorption enhancement hints at the occurrence of Mahan excitons. Furthermore, IVB transitions become possible when holes scatter to the edges of the Brillouin zone, their fast response time renders them interesting for optoelectronic switching devices. Finally, there is evidence for hot-phonon effects, from both a delayed charge-carrier relaxation and an increase in the exciton–phonon-complex energy. The described dynamics are crucially dependent on the pump wavelength and hence the excess energy obtained by the carriers which determines their effective temperature. From our data we can also conclude that the high density of hot charge carriers does not trigger the Mott transition. The survival of the excitonic absorption reflects directly the non-equilibrium distribution of the highly excited charge carriers. These results stimulate a demand for the development of new theories describing high-density exciton systems beyond the present state.

Acknowledgments

We thank Peter Schlupp for growing the thin film and Michael Lorenz (both Universität Leipzig) for x-ray diffraction measurements. We gratefully acknowledge valuable discussions with Christoph Cobet, Martin Feneberg, Daniel Franta, Kurt Hingerl, Michael Lorke, Bernd Rheinländer, Chris Sturm and Marcel Wille, and lab support by Martin Přeček. Parts of this work have been funded by the Deutsche Forschungsgemeinschaft (DFG, German Research Foundation), SFB 762 - Projektnr. 31047526 (project B03), and FOR 1616 (SCHM2710/2). OH acknowledges the Leipzig School of Natural Sciences BuildMoNa. Experimental development at ELI Beamlines was funded by the project 'Advanced research using high intensity laser produced photons and particles' (ADONIS), Reg. No. CZ.02.1.01/0.0/0.0/16_019/0000789, from the European Regional Development Fund, and the National Program of Sustainability II project 'ELI Beamlines - International Center of Excellence' (ELISus), project code: LQ1606. SE was partially supported by the project 'Structural dynamics of biomolecular systems' (ELIBIO), reg. No. CZ.02.1.01/0.0/0.0/15_003/0000447, from the European Regional Development Fund. JA acknowledges support of the Ministry of Education, Youth and Sports as part of targeted support from the National Programme of Sustainability II and the Chalmers Area of Advanced Materials Science. JAL and AS were supported by the National Science Foundation under Grant Nos. DMR-1555153 and CBET-1437230, and computer time was provided as part of the Blue Waters sustained-petascale computing project, which is supported by the National Science Foundation (awards OCI-0725070 and ACI-1238993) and the state of Illinois. SZ was supported by the National Science Foundation, Grant No. DMR-1505172.

ORCID iDs

Steffen Richter  <https://orcid.org/0000-0001-7344-1518>
Oliver Herrfurth  <https://orcid.org/0000-0002-7777-0885>
Shirly Espinoza  <https://orcid.org/0000-0002-2740-7156>
Mateusz Rebarz  <https://orcid.org/0000-0002-5823-2432>
Miroslav Kloz  <https://orcid.org/0000-0003-4609-8018>
Joshua A Leveillee  <https://orcid.org/0000-0003-2393-3973>
André Schleife  <https://orcid.org/0000-0003-0496-8214>
Stefan Zollner  <https://orcid.org/0000-0001-7752-7941>
Marius Grundmann  <https://orcid.org/0000-0001-7554-182X>
Jakob Andreasson  <https://orcid.org/0000-0002-3202-2330>
Rüdiger Schmidt-Grund  <https://orcid.org/0000-0002-9655-9479>

References

- [1] Chemla D S and Shah J 2001 Many-body and correlation effects in semiconductors *Nature* **414** 549–57
- [2] Huber R, Tauser F, Brodschelm A, Bichler M, Abstreiter G and Leitenstorfer A 2001 How many-particle interactions develop after ultrafast excitation of an electron–hole plasma *Nature* **414** 286–9
- [3] Fleming G R and Ratner M A 2008 Grand challenges in basic energy sciences *Phys. Today* **61** 28–33
- [4] Baldini E et al 2017 Real-time observation of phonon-mediated σ - π interband scattering in MgB₂ *Phys. Rev. Lett.* **119** 097002
- [5] Winkler T, Haahr-Lillevang L, Sarpe C, Zielinski B, Götze N, Senfleben A, Balling P and Baumert T 2017 Laser amplification in excited dielectrics *Nat. Phys.* **14** 74–9
- [6] Nenstiel C et al 2018 Electronic excitations stabilized by a degenerate electron gas in semiconductors *Commun. Phys.* **1** 38
- [7] Versteegh M A M, van Lange A J, Stoof H T C and Dijkhuis J I 2012 Observation of preformed electron–hole Cooper pairs in highly excited ZnO *Phys. Rev. B* **85** 195206
- [8] Colman P, Lunnemann P, Yu Y and Mørk J 2016 Ultrafast coherent dynamics of a photonic crystal all-optical switch *Phys. Rev. Lett.* **117** 233901
- [9] Chai Z, Hu X, Wang F, Niu X, Xie J and Gong Q 2017 Ultrafast all-optical switching *Adv. Opt. Mater.* **5** 1600665
- [10] Mashiko H, Oguri K, Yamaguchi T, Suda A and Gotoh H 2016 Petahertz optical drive with wide-bandgap semiconductor *Nat. Phys.* **12** 741–5
- [11] Athale R and Psaltis D 2016 Optical computing: past and future *Opt. Photon. News* **27** 32–9
- [12] Ohta H and Hosono H 2004 Transparent oxide optoelectronics *Mater. Today* **7** 42–51
- [13] Frenzel H, Lajn A, von Wenckstern H, Lorenz M, Schein F, Zhang Z and Grundmann M 2010 Recent progress on ZnO-based metal-semiconductor field-effect transistors and their application in transparent integrated circuits *Adv. Mater.* **22** 5332–49
- [14] Ponseca C S Jr, Chábera P, Uhlig J, Persson P and Sundström V 2017 Ultrafast electron dynamics in solar energy conversion *Chem. Rev.* **117** 10940–1024
- [15] Kahmann S and Loi M A 2019 Hot carrier solar cells and the potential of perovskites for breaking the Shockley–Queisser limit *J. Mater. Chem. C* **7** 2471
- [16] Atwater H A, Davoyan A R, Ilic O, Jariwala D, Sherrott M C, Went C M, Whitney W S and Wong J 2018 Materials challenges for the starshot lightsail *Nat. Mater.* **17** 861–7
- [17] Sundaram S K and Mazur E 2002 Inducing and probing non-thermal transitions in semiconductors using femtosecond laser pulses *Nat. Mat.* **1** 217–24

- [18] Lorenz M et al 2016 The 2016 oxide electronic materials and oxide interfaces roadmap *J. Phys. D: Appl. Phys.* **49** 433001
- [19] Mor S et al 2017 Ultrafast electronic band gap control in an excitonic insulator *Phys. Rev. Lett.* **119** 086401
- [20] Zong A et al 2019 Evidence for topological defects in a photoinduced phase transition *Nat. Phys.* **15** 27–31
- [21] Dönges S A, Sven A, Khatib O, O’Callahan B T, Atkin J M, Park J H, Cobden D and Raschke M B 2016 Ultrafast nanoimaging of the photoinduced phase transition dynamics in VO₂ *Nano Lett.* **16** 3029–35
- [22] Zürich M et al 2017 Direct and simultaneous observation of ultrafast electron and hole dynamics in germanium *Nat. Commun.* **8** 15734
- [23] Ziája B, Medvedev N, Tkachenko V, Maltezopoulos T and Wurth W 2015 Time-resolved observation of band-gap shrinking and electron-lattice thermalization within x-ray excited gallium arsenide *Sci. Rep.* **5** 18068
- [24] Eisele M, Cocker T L, Huber M A, Plankl M, Viti L, Ercolani D, Sorba L, Vitiello M S and Huber R 2014 Ultrafast multi-terahertz nano-spectroscopy with sub-cycle temporal resolution *Nat. Photon.* **8** 841
- [25] Foglia L, Wolf M and Stähler J 2016 Ultrafast dynamics in solids probed by femtosecond time-resolved broadband electronic sum frequency generation *Appl. Phys. Lett.* **109** 202106
- [26] Shah J 1999 *Ultrafast Spectroscopy of Semiconductors and Semiconductor Nanostructures* (Springer Series in Solid-State Sciences vol 115) 2nd edn (Berlin: Springer)
- [27] Bohnert K, Schmieder G and Klingshirn C 1980 Gain and reflection spectroscopy and the present understanding of the electron-hole plasma in II–VI compounds *Phys. Status Solidi B* **98** 175–88
- [28] Huang L, Callan J P, Glezer E N and Mazur E 1998 GaAs under intense ultrafast excitation: response of the dielectric function *Phys. Rev. Lett.* **80** 185
- [29] Roeser C A D, Kim A M-T, Callan J P, Huang L, Glezer E N, Siegal Y and Mazur E 2003 Femtosecond time-resolved dielectric function measurements by dual-angle reflectometry *Rev. Sci. Instrum.* **74** 3413–22
- [30] Shih T, Winkler M T, Voss T and Mazur E 2009 Dielectric function dynamics during femtosecond laser excitation of bulk ZnO *Appl. Phys. A* **96** 363–7
- [31] Boschini F, Hedayat H, Piovera C, Dallera C, Gupta A and Carpena E 2015 A flexible experimental setup for femtosecond time-resolved broad-band ellipsometry and magneto-optics *Rev. Sci. Instrum.* **86** 013909
- [32] Baldini E, Mann A, Borroni S, Arrell C, van Mourik F and Carbone F 2016 A versatile setup for ultrafast broadband optical spectroscopy of coherent collective modes in strongly correlated quantum systems *Struct. Dyn.* **3** 064301
- [33] Hiramatsu K and Nagata T 2015 Communication: broadband and ultrasensitive femtosecond time-resolved circular dichroism spectroscopy *J. Chem. Phys.* **143** 121102
- [34] Poellmann C et al 2015 Resonant internal quantum transitions and femtosecond radiative decay of excitons in monolayer WSe₂ *Nat. Mater.* **14** 889–93
- [35] Klingshirn C F, Meyer B K, Waag A, Hoffmann A and Geurts J 2010 *Zinc Oxide* (Springer Series in Materials Science) (Berlin: Springer)
- [36] Shokhovets S, Ambacher O, Meyer B K and Gobsch G 2008 Anisotropy of the momentum matrix element, dichroism, and conduction-band dispersion relation of wurtzite semiconductors *Phys. Rev. B* **78** 035207
- [37] Oki K and Ishitani Y 2019 Influence of LO and LA phonon processes on thermal-nonequilibrium excitation and deexcitation dynamics of excitons in GaN, AlN, and ZnO *J. Appl. Phys.* **125** 205705
- [38] Choo H R, Hu X F, Downer M C and Kesan V P 1993 Femtosecond ellipsometric study of nonequilibrium carrier dynamics in Ge and epitaxial Si_{1-x}Ge_x *Appl. Phys. Lett.* **63** 1507–9
- [39] Zollner S, Myers K D, Jensen K G, Dolan J M, Bailey D W and Stanton C J 1997 Femtosecond interband hole scattering in Ge studied by pump-probe reflectivity *Solid State Commun.* **104** 51–5
- [40] Yoneda H, Morikami H, Ueda K-I and More R M 2003 Ultrashort-pulse laser ellipsometric pump-probe experiments on gold targets *Phys. Rev. Lett.* **91** 075004
- [41] Kruglyak V V, Hicken R J, Ali M, Hickey B J, Pym A T G and Tanner B K 2005 Measurement of hot electron momentum relaxation times in metals by femtosecond ellipsometry *Phys. Rev. B* **71** 233104
- [42] Mounier D, Morozov E, Ruello P, Breteau J-M, Picart P and Gusev V 2008 Detection of shear picosecond acoustic pulses by transient femtosecond polarimetry *Eur. Phys. J. Spec. Top.* **153** 243–6
- [43] Min C-K, Cahill D G and Granick S 2010 Time-resolved ellipsometry for studies of heat transfer at liquid/solid and gas/solid interfaces *Rev. Sci. Instrum.* **81** 074902
- [44] Rapp S, Kaiser M, Schmidt M and Huber H P 2016 Ultrafast pump-probe ellipsometry setup for the measurement of transient optical properties during laser ablation *Opt. Express* **24** 17572–92
- [45] Csontos J, Toth Z, Pápa Z, Gábor B, Füle M, Gilicze B and Budai J 2017 Ultrafast *in situ* null-ellipsometry for studying pulsed laser—silicon surface interactions *Appl. Surf. Sci.* **421** 325–30
- [46] Pflug T, Wang J, Olbrich M, Frank M and Horn A 2018 Case study on the dynamics of ultrafast laser heating and ablation of gold thin films by ultrafast pump-probe reflectometry and ellipsometry *Appl. Phys. A* **124** 116
- [47] Pal D, Singhal J, Mathur A, Singh A, Dutta S, Zollner S and Chattopadhyay S 2017 Effect of substrates and thickness on optical properties in atomic layer deposition grown ZnO thin films *Appl. Surf. Sci.* **421** 341
- [48] Samarasingha N S, Zollner S, Pal D, Singh R and Chattopadhyay S 2020 Thickness dependence of infrared lattice absorption and excitonic absorption in ZnO layers on Si and SiO₂ grown by atomic layer deposition *J. Vac. Sci. Technol. B* **38** 042201
- [49] Reřbarz M, Kloz M, Espinoza Herrera S J and Brooks C D 2017 UV-VIS-NIR Femtosekundový Elipsometrický Systém, Užžitný Vzor 30838 (Česká Republika: Úřad Průmyslového Vlastnictví)
- [50] Espinoza S, Richter S, Reřbarz M, Herrfurth O, Schmidt-Grund R, Andreasson J and Zollner S 2019 Transient dielectric functions of Ge, Si, and InP from femtosecond pump-probe ellipsometry *Appl. Phys. Lett.* **115** 052105
- [51] Herrfurth O, Pflug T, Olbrich M, Grundmann M, Horn A and Schmidt-Grund R 2019 Femtosecond-time-resolved imaging of the dielectric function of ZnO in the visible to near-IR spectral range *Appl. Phys. Lett.* **115** 212103
- [52] Schubert M 1996 Polarization-dependent optical parameters of arbitrarily anisotropic homogeneous layered systems *Phys. Rev. B* **53** 4265–74
- [53] Johs B and Hale J S 2008 Dielectric function representation by B-splines *Phys. Status Solidi A* **205** 715–9
- [54] Shokhovets S, Spieß L and Gobsch G 2010 Spectroscopic ellipsometry of wurtzite ZnO and GaN: examination of a special case *J. Appl. Phys.* **107** 023509
- [55] Likhachev D V 2017 Selecting the right number of knots for B-spline parameterization of the dielectric functions in spectroscopic ellipsometry data analysis *Thin Solid Films* **636** 519–26
- [56] Hohenberg P and Kohn W 1964 Inhomogeneous electron gas *Phys. Rev.* **136** 864–71

- [57] Kohn W and Sham L J 1965 Self-consistent equations including exchange and correlation effects *Phys. Rev.* **140** A1133–8
- [58] Onida G, Reining L and Rubio A 2002 Electronic excitations: density-functional versus many-body Green's-function approaches *Rev. Mod. Phys.* **74** 601
- [59] Gajdoš M, Hummer K, Kresse G, Furthmüller J and Bechstedt F 2006 Linear optical properties in the projector-augmented wave methodology *Phys. Rev. B* **73** 045112
- [60] Kresse G and Joubert D 1999 From ultrasoft pseudopotentials to the projector augmented-wave method *Phys. Rev. B* **59** 1758–75
- [61] Kresse G and Furthmüller J 1996 Efficient iterative schemes for *ab initio* total-energy calculations using a plane-wave basis set *Phys. Rev. B* **54** 11169–86
- [62] Schleife A, Rödl C, Fuchs F, Furthmüller J and Bechstedt F 2009 Optical and energy-loss spectra of MgO, ZnO, and CdO from *ab initio* many-body calculations *Phys. Rev. B* **80** 035112
- [63] Schleife A, Rödl C, Fuchs F, Hannewald K and Bechstedt F 2011 Optical absorption in degenerately doped semiconductors: Mott transition or Mahan excitons? *Phys. Rev. Lett.* **107** 236405
- [64] Rödl C, Fuchs F, Furthmüller J and Bechstedt F 2008 *Ab initio* theory of excitons and optical properties for spin-polarized systems: application to antiferromagnetic MnO *Phys. Rev. B* **77** 184408
- [65] Fuchs F, Rödl C, Schleife A and Bechstedt F 2008 Efficient $\mathcal{O}(N^2)$ approach to solve the Bethe–Salpeter equation for excitonic bound states *Phys. Rev. B* **78** 085103
- [66] Berggren K-F and Sernelius B E 1981 Band-gap narrowing in heavily doped many-valley semiconductors *Phys. Rev. B* **24** 1971–86
- [67] Wu J, Walukiewicz W, Shan W, Yu K M, Ager J W, Haller E E, Lu H and Schaff W J 2002 Effects of the narrow band gap on the properties of InN *Phys. Rev. B* **66** 201403
- [68] Kronenberger A, Polity A, Hofmann D M, Meyer B K, Schleife A and Bechstedt F 2012 Structural, electrical, and optical properties of hydrogen-doped ZnO films *Phys. Rev. B* **86** 115334
- [69] Bechstedt F 2015 *Electron–Hole Problem* (Berlin: Springer) pp 439–57
- [70] Schleife A 2011 *Electronic and Optical Properties of MgO, ZnO, and CdO* (Saarbrücken: Südwestdeutscher Verlag für Hochschulschriften)
- [71] Kang K, Kononov A, Lee C-W, Leveille J A, Shapera E P, Zhang X and Schleife A 2019 Pushing the frontiers of modeling excited electronic states and dynamics to accelerate materials engineering and design *Comput. Mater. Sci.* **160** 207–16
- [72] Othonos A 1998 Probing ultrafast carrier and phonon dynamics in semiconductors *J. Appl. Phys.* **83** 1789
- [73] Gattass R R and Mazur E 2008 Femtosecond laser micromachining in transparent materials *Nat. Photon.* **2** 219–25
- [74] Mao S S, Quéré F, Guizard S, Mao X, Russo R E, Petite G and Martin P 2004 Dynamics of femtosecond laser interactions with dielectrics *Appl. Phys. A* **79** 1695–709
- [75] Segura A, Bouvier J, Andrés M V, Man'ón F J and Muñoz V 1997 Strong optical nonlinearities in gallium and indium selenides related to inter-valence-band transitions induced by light pulses *Phys. Rev. B* **56** 4075–84
- [76] Lao Y-F and Unil Perera A G 2011 Dielectric function model for p-type semiconductor inter-valence band transitions *J. Appl. Phys.* **109** 103528
- [77] Allen M W, Swartz C H, Myers T H, Veal T D, McConville C F and Durbin S M 2010 Bulk transport measurements in ZnO: the effect of surface electron layers *Phys. Rev. B* **81** 075211
- [78] Foglia L, Vempati S, Bonkano B T, Gierster L, Wolf M, Sadofev S and Stähler J 2019 Revealing the competing contributions of charge carriers, excitons, and defects to the non-equilibrium optical properties of ZnO *Struct. Dyn.* **6** 034501
- [79] Stölzel M, Kupper J, Brandt M, Müller A, Benndorf G, Lorenz M and Grundmann M 2012 Electronic and optical properties of ZnO/(Mg, Zn)O quantum wells with and without a distinct quantum-confined Stark effect *J. Appl. Phys.* **111** 063701
- [80] Shah J 1978 Hot electrons and phonons under high intensity photoexcitation of semiconductors *Solid-State Electron.* **21** 43–50
- [81] Hess S, Taylor R A, O'Sullivan E D, Ryan J F, Cain N J, Roberts V and Roberts J S 1999 Hot carrier relaxation by extreme electron–LO phonon scattering in GaN *Phys. Status Solidi B* **216** 51–5
- [82] Sadasivam S, Chan M K Y and Darancet P 2017 Theory of thermal relaxation of electrons in semiconductors *Phys. Rev. Lett.* **119** 136602
- [83] Grundmann M 2016 *The Physics of Semiconductors: An Introduction Including Nanophysics and Applications* 3rd edn (Berlin: Springer)
- [84] Chen C, Dutta M and Stroschio M A 2004 Electron scattering via interactions with optical phonons in wurtzite crystals *Phys. Rev. B* **70** 075316
- [85] Das Sarma S, Jain J K and Jalabert R 1988 Theory of hot-electron energy loss in polar semiconductors: role of plasmon–phonon coupling *Phys. Rev. B* **37** 6290–6
- [86] Pötz W and Kocevar P 1983 Electronic power transfer in pulsed laser excitation of polar semiconductors *Phys. Rev. B* **28** 7040–7
- [87] von der Linde D, Kuhl J and Klingenberg H 1980 Raman scattering from nonequilibrium LO phonons with picosecond resolution *Phys. Rev. Lett.* **44** 1505–8
- [88] Sjodin T, Petek H and Dai H-L 1998 Ultrafast carrier dynamics in silicon: a two-color transient reflection grating study on a (111) surface *Phys. Rev. Lett.* **81** 5664–7
- [89] Yoffa E J 1981 Screening of hot-carrier relaxation in highly photoexcited semiconductors *Phys. Rev. B* **23** 1909–19
- [90] Seymour R J, Junnarkar M R and Alfano R R 1982 Slowed picosecond kinetics of hot photogenerated carriers in GaAs *Solid State Commun.* **41** 657–60
- [91] Ehrenreich H 1959 Screening effects in polar semiconductors *J. Phys. Chem. Solids* **8** 130–5
- [92] Alfano R R (ed) 1984 *Semiconductors Probed by Ultrafast Laser Spectroscopy* (New York: Academic)
- [93] Leheny R F, Shah J, Fork R L, Shank C V and Migus A 1979 Dynamics of hot carrier cooling in photo-excited GaAs *Solid State Commun.* **31** 809–13
- [94] Ishioka K, Petek H, Kaydashev V E, Kaidashev E M and Misochko O V 2010 Coherent optical phonons of ZnO under near resonant photoexcitation *J. Phys. Condens. Matter* **22** 465803
- [95] Lin J-H et al 2016 Coherent acoustic phonon oscillation accompanied with backward acoustic pulse below exciton resonance in a ZnO epilayer on oxide-buffered Si(111) *J. Phys. D: Appl. Phys.* **49** 325102
- [96] Baldini E, Dominguez A, Palmieri T, Cannelli O, Rubio A, Ruello P and Chergui M 2019 Exciton control in a room temperature bulk semiconductor with coherent strain pulses *Sci. Adv.* **5** eaax2937
- [97] Cho G C, Kütt W and Kurz H 1990 Subpicosecond time-resolved coherent-phonon oscillations in GaAs *Phys. Rev. Lett.* **65** 764–6

- [98] Ou P C, Lin J H and Hsieh W F 2012 Spectral dependence of transient reflectance in a ZnO epitaxial film at room temperature *Appl. Phys. B* **106** 399–404
- [99] Rai R C, Guminiak M, Wilser S, Cai B and Nakarmi M L 2012 Elevated temperature dependence of energy band gap of ZnO thin films grown by e-beam deposition *J. Appl. Phys.* **111** 073511
- [100] Gay J G 1971 Screening of excitons in semiconductors *Phys. Rev. B* **4** 2567–75
- [101] Klingshirn C and Haug H 1981 Optical properties of highly excited direct gap semiconductors *Phys. Rep.* **70** 315–98
- [102] Zimmermann R 1988 Nonlinear optics and the Mott transition in semiconductors *Phys. Status Solidi B* **146** 371–84
- [103] Yamamoto A, Kido T, Goto T, Chen Y, Yao T and Kasuya A 1999 Dynamics of photoexcited carriers in ZnO epitaxial thin films *Appl. Phys. Lett.* **75** 469–71
- [104] Acharya S, Chouthe S, Graener H, Böntgen T, Sturm C, Schmidt-Grund R, Grundmann M and Seifert G 2014 Ultrafast dynamics of the dielectric functions of ZnO and BaTiO₃ thin films after intense femtosecond laser excitation *J. Appl. Phys.* **115** 053508
- [105] Klingshirn C F 2012 *Semiconductor Optics* (Berlin: Springer)
- [106] Klingshirn C, Hauschild R, Fallert J and Kalt H 2007 Room-temperature stimulated emission of ZnO: alternatives to excitonic lasing *Phys. Rev. B* **75** 115203
- [107] Versteegh M A M, Kuis T, Stoof H T C and Dijkhuis J T 2011 Ultrafast screening and carrier dynamics in ZnO: theory and experiment *Phys. Rev. B* **84** 035207
- [108] Mahan G D 1967 Excitons in degenerate semiconductors *Phys. Rev.* **153** 882–9
- [109] Haug H and Tran T D B 1978 Dynamical screening of excitons by free carriers *Phys. Status Solidi B* **85** 561–8
- [110] Palmieri T, Baldini E, Steinhoff A, Akrap A, Kollár M, Horváth E, Forró L, Jahnke F and Chergui M 2020 Mahan excitons in room-temperature methylammonium lead bromide perovskites *Nat. Commun.* **11** 850
- [111] Bachmann M, Czerner M, Edalati-Boostan S and Heiliger C 2012 *Ab initio* calculations of phonon transport in ZnO and ZnS *Eur. Phys. J. B* **85** 146
- [112] Hendry E, Koeberg M and Bonn M 2007 Exciton and electron–hole plasma formation dynamics in ZnO *Phys. Rev. B* **76** 045214
- [113] Schmidt F, Müller S, von Wenckstern H, Dietrich C P, Heinhold R, Kim H-S, Allen M W and Grundmann M 2013 Comparative study of deep defects in ZnO microwires, thin films and bulk single crystals *Appl. Phys. Lett.* **103** 062102
- [114] Franta D, Nečas D and Zajíčková L 2013 Application of Thomas–Reiche–Kuhn sum rule to construction of advanced dispersion models *Thin Solid Films* **534** 432–41